1 **Experimental investigation of Apollo 16 "Rusty Rock" formation by a**

2 **lunar fumarolic gas**

3 C. J. Renggli[1], S. Klemme[1]

4 [1] Institut für Mineralogie, Universität Münster, Münster, 48149, Deutschland

5 Corresponding author: Christian Renggli (renggli@uni-muenster.de)

6 ORCID: Renggli 0000-0001-8913-4176

7 ORCID: Klemme 0000-0001-7859-9779

8

Key points

10 - Experiments constrain the temperature of Apollo 16 "rusty rock" alteration to
11   580 ± 50 °C.

12 - Gas deposition and gas-solid metal reaction experiments reproduce the "rusty rock"
13   alteration phases $FeCl_2$ and $(Zn,Fe)S$

Abstract

14

15   The Apollo 16 sample 66095, named "rusty rock", is uniquely enriched in volatile and

16   moderately volatile elements. The impact melt breccia is characterized by the abundant occurrence of

17   Fe-rich sulfide and chloride alteration phases, including FeS, ZnS and $FeCl_2$. These phases have

18   previously been interpreted to be the result of fumarolic alteration of the breccia. Here we present the

19   results of two different experimental approaches, which aim to constrain the temperature conditions

20   and the process under which the "rusty rock" alteration formed. The first experimental set-up assumes

21   that the metals Zn, Cu and Fe were introduced into the rock by a C-O-S-Cl gas phase, and that the Fe-

22   rich sulfides and chlorides were deposited from this gas phase. This "gas deposition" experiment

23   suggests that the alteration assemblage formed over the temperature range of 538-638 °C. The second

24   experimental set-up simulates a scenario, where Fe metal particles in the lunar rock react with a Zn-C-

25   O-S-Cl gas phase at six different temperatures between 396 °C and 1005 °C. This latter "metal

26   reaction" experiment resulted in the formation of sulfide and chloride coatings on the Fe metal chips.

27   The "rusty rock" alteration phases $FeCl_2$ and (Zn,Fe)S were abundantly present in the coating of the

28   Fe metal chip reacted at 580 °C. Both experiments lead to results which are in agreement, providing a

29   temperature of 580 ± 50 °C for the fumarolic alteration on the Moon, as observed in the Apollo 16

30   "rusty rock".

Plain Language Summary

31

32   The Apollo 16 sample 66095, named "rusty rock", is a rare lunar rock which is enriched in

33   volatile elements such as sulfur and chlorine. We investigate two processes by which sulfides and

34   chlorides may form in a lunar fumarolic system, by conducting experiments in evacuated silica glass

35   tubes at reducing conditions. First, we assume that metals and volatiles (Zn, Cu, Fe, S and Cl) are

36   deposited from a gas phase (gas deposition experiments), and second, we assume that Fe metal is

37   already present in the rock and altered by the introduction of a Zn-S-Cl-bearing gas phase (metal

38   reaction experiment). In both experimental setups we observe the formation of "rusty rock" alteration

39   phases FeCl$_2$ and (Zn,Fe)S at 580 ± 50 °C, constraining the temperature of fumarolic alteration

40   recorded in the Apollo 16 sample 66095.

1. Introduction

42   The Apollo 16 "rusty rock" 66095 is a unique lunar sample which is highly enriched in the

43   volatile elements S and Cl and in moderately volatile trace metals such as Tl, Br, Cd, Sn, Zn, Pb, Rb,

44   Cs, Ga, B and Li (Krähenbühl et al., 1973; Taylor et al., 1973; Shearer et al., 2014; Day et al., 2017;

45   Day et al., 2019). This is in contrast to the vast majority of lunar samples which are generally very

46   volatile depleted (e.g. McCubbin et al., 2015).

47   Sample 66095 is a fine-grained impact melt breccia with lithic clasts, including anorthosite,

48   troctolite, basalt and a minor KREEP-like component. The lithic clasts further contain metallic iron-

49   nickel grains. These grains are commonly altered on the rims to (Fe,Ni)Cl$_2$, FeO(OH,Cl), FeS and

50   occasional ZnS (Taylor et al., 1973; El Goresy et al., 1973; Taylor et al., 1974; Hunter and Taylor,

51   1981a; Hunter and Taylor, 1981b; Shearer et al., 2014). The alteration occurs on the surface of the

52   rocks as well as the interior, suggesting that it was not a secondary process that occurred after

53   sampling in the spacecraft or on Earth (Meyer, 2009). Similar alteration features were observed in

54   more than 20 different Apollo 16 samples (Taylor et al., 1973; Jean et al., 2016). This suggests that

55   the alteration is a regional lunar process, rather than an extraordinary process limited to sample 66095.

56   Sulfide alteration is not only associated with FeNi grains, but it also occurs disseminated in veins and

57   replacement textures of olivine and pyroxene in Apollo 16 rocks (Norman, 1981; Colson, 1992;

58   Norman et al., 1995; Shearer et al., 2012). This underlines the broader importance of the "rusty rock",

59   which provides a unique insight into the transport of volatile elements in the lunar crust.

60   Recent work has highlighted unique isotopic signatures of the Apollo 16 "rusty rock" 66095

61   (Shearer et al., 2014; Day et al., 2017; Day et al., 2019). The "rusty rock" is one of the most S-rich

62   Apollo 16 samples, and with $\delta^{34}S$=+1.9‰ one of the most isotopically light lunar samples (Kerridge

63   et al., 1975). Other lunar samples with light $\delta^{34}S$ compositions include volatile coatings on Apollo 17

64   pyroclastic glass beads and troilite replacement veins in Apollo 16 breccias (Shearer et al., 2012).

65　Because the light S isotopes preferentially partition into the gas phase, isotopically light δ^{34}S in 66095

66　sulfides indicate that they deposited from a volcanic or fumarolic gas (Shearer et al., 2012; Shearer et

67　al., 2014). The Cl isotopic composition of 66095, on the other hand, is heavy with respect to lunar

68　igneous rocks, with δ^{37}Cl ranging from +14.0‰ to +15.6‰ (Sharp et al., 2010; Shearer et al., 2014).

69　With the exception of some lunar apatites (Wang et al., 2012), these are the heaviest Cl isotopic

70　compositions measured in lunar samples (Shearer et al., 2014). As the overall Cl isotopic composition

71　of the Moon was inferred to be similar to that of the Earth, the occurrence of much heavier isotopic

72　compositions was attributed to the volatilization of metal halides (Sharp et al., 2010; Shearer et al.,

73　2014). These metal halides were deposited from the gas phase on pyroclastic glass beads, and in

74　altered regolith and breccia such as 66095. The isotopic composition of Zn supports the interpretation

75　of S and Cl isotopic compositions and the δ^{66}Zn composition of the "rusty rock" reveals the lightest

76　isotopic signature of Zn recorded in any sample analyzed, with δ^{66}Zn = -13.7‰ (Day et al., 2017).

77　This light isotopic signature was interpreted to be caused by degassing from a volatile-depleted Moon

78　and condensation in the lunar regolith and on the Moon's surface (Day et al., 2017; Day et al., 2019).

79　Note that Cu and Fe isotopic compositions of 66095 are not fractionated and are within the range of

80　normal lunar mare basalts (δ^{65}Cu = 0.9‰, δ^{56}Fe = 0.1‰) (Day et al., 2019). Iron is considered a non-

81　volatile element but Cu is quite volatile (Lodders, 2003; Norris and Wood, 2017; Sossi and Fegley,

82　2018; Sossi et al., 2019) so that stable Cu isotopes should have been fractionated if Cu had been

83　deposited from a gas phase in the "rusty rock".

84　　　　Two different mechanisms are conceivable for the formation of the observed sulfide and

85　chloride alteration in the "rusty rock" samples. In the first scenario, all metals (i.e., Zn, Cu and Fe)

86　together with S and Cl were introduced into the rock by a fumarolic gas phase and this caused

87　deposition of metal sulfides and chlorides. This process would be recorded in the rock by light

88　isotopic signatures of the metals and the isotopically light Zn isotopes support this process (Day et al.,

89　2017). However, the Cu and Fe isotopes are not isotopically light (Day et al., 2019) and hence this

90　process does not account for the Cu and Fe isotopes. In a second scenario, the metals Fe and Cu were

91　not introduced by the gas phase, but instead, they were present in the rock prior to gas metasomatism

92   and hence the metals Cu and Fe reacted with a gas phase to form sulfides and chlorides. Based on the

93   isotopic composition the latter mechanism was proposed to explain the alteration of Cu and Fe in the

94   "rusty rock" (Day et al., 2019)

95   Here, we experimentally simulate both mechanisms in the laboratory and aim to constrain the

96   temperature conditions at which the rusty alteration phases, including lawrencite, sphalerite and

97   troilite formed. Furthermore, we aim to put constraints on fumarolic gas composition and test if the

98   two mechanisms discussed above are viable. For this purpose we used two different experimental

99   approaches, where the first approach assumes that all major elements of the alteration assemblage

100   (i.e., Zn, Fe, Cu, Cl and S) were transported by a gas phase to form deposits along a temperature

101   gradient (gas deposition experiment), essentially identical to the formation of mineral deposits from

102   fumarolic gases. The second approach assumes that the Fe metal was already present in the rock and

103   only Zn, Cl and S were introduced by a gas phase, which reacted with the metal to form the alteration

104   assemblage (metal reaction experiment).

2. Methods

106   We conducted two different gas-solid reaction experiments in evacuated silica glass tubes

107   (Fig. 1). The first type of experiments, which we call "gas deposition experiments", simulates the

108   transport of Zn, Cu and Fe in a C-O-S-Cl gas and the resulting deposition of sulfide and chloride

109   phases. A mixture of ZnO, FeS, CuS, $MgCl_2$ and C in the relative molar abundance of 1-1-1-3-4 was

110   prepared as a 50 mg pellet and placed in an open graphite crucible (Table 1), which was then placed at

111   the bottom of a 30 cm long evacuated silica glass tube.

112   In the second type of experiments, which we call "metal reaction experiments", we

113   investigated the reaction of Fe metal with a Zn-C-O-S-Cl gas phase at 396, 496, 580, 708, 825 and

114   1005 °C (Table 2). A pellet containing a mixture of ZnO, $MgCl_2$, S and C in the relative molar

115   abundance of 1-1-1-4 (Table 1) was prepared in an open graphite crucible and placed in the evacuated

116   silica glass tube. Iron metal chips with diameters of ~ 1 mm were placed on silica glass wool spacers

117   along the tube prior to the evacuation of the tube.

118   Both experiments were conducted in evacuated and sealed silica glass tubes at an internal

119   pressure of 10^{-5} bar. The silica glass tubes were suspended in a vertical tube furnace (Gero GmbH,

120   Germany), set to 1250 °C, sealed at the top and at the bottom to avoid convection. The furnace had a

121   temperature gradient of 900 °C from the hot zone to the top of the silica glass tube (Fig. 1). The pellet

122   mixtures reacted at high temperature (1250 °C) to form a gas phase that subsequently moved upwards

123   along the temperature gradient over the duration of the 24-hour experiments. The graphite crucible

124   and the carbon added to the mixtures acted as a reducing agent buffering the gas mixture at the C-CO

125   buffer at the source.

126   The silica glass tubes were lifted out of the furnace, quenched in water and cut in 1cm long

127   segments. The samples were immediately placed in an evacuated desiccator in order to avoid

128   alteration by exposure to the humidity in the air (Dalby et al., 2018). Aliquots of the reacted Fe metal

129   chips were embedded in epoxy resin and prepared as polished cross-sections. The mounts were

130   polished dry without water to avoid hydration of the samples.

131   All samples were analyzed with a JSM-6610 Series Scanning Electron Microscope (SEM).

132   The silica tube segments with the sulfide and chloride deposits on the inner silica glass tube wall were

133   analyzed without carbon coating using the low-vacuum capability of the SEM at 50 Pa. This allowed

134   a minimization of sample exposure to ambient air and modification during sample preparation. The

135   cross-sectioned samples were carbon coated and analyzed and imaged at high-vacuum using the

136   Back-Scattered Electron (BSE) detector. All EDS analysis were done at an acceleration voltage of 20

137   kV and a working distance of 10 mm, using the JEOL EDS analysis station with a dry silicon drift

138   detector.

139   **3. Results**

140   **3.1 Gas deposition experiments**

141   We observe eight different phases deposited on the inner wall of the silica glass tube, over the

142   entire temperature range from 330-1250 °C (Fig. 2). With the exception of forsterite (Mg_2SiO_4),

143   which forms as the product of a reaction of the starting material with the silica glass tube, the phases

144   were deposited from the Zn-Fe-Cu-C-O-S-Cl gas. We observe forsterite only at high temperatures

145   (T > 698 °C) with grain sizes of up to 20 μm. Phases deposited from the gas phase are spread over

146   almost the entire silica tube from 330-1140 °C, with little overlap of different phases (Fig. 3). The

147   only chemical compound remaining in the graphite crucible after the experiment is MgO. The MgO

148   forms a dense pellet with grain sizes of up to 20 μm.

149   Chalcocite (Cu_2S) occurs between 878-1140 °C and forms tabular grains often deposited in

150   patches or groups of multiple single crystals (Fig. 2a & b). Below 1000 °C the crystals form

151   increasingly well-developed crystal faces, whereas the typical habit of chalcocite crystals is more

152   rounded at higher temperatures, especially when T approaches the melting point of Cu_2S at 1130 °C.

153   The crystals have diameters of up to 60 μm and are commonly associated with higher abundances of

154   forsterite on the tube wall. All chalcocite crystals show the growth of Cu-metal whiskers extruding

155   from their surface (Fig. 2b). The whiskers have lengths of up to 10 μm and are composites of copper

156   fibers with sub-micron diameters. At 698-830 °C (Fig. 3) we observe an unidentified Fe-Cu-S-Cl

157   phase. These rare crystals have diameters of ~40 μm and well-developed triangular crystal faces.

158   The largest quantities of metal sulfide and chloride deposits occur over the relatively narrow

159   temperature range of 540-700 °C (Fig. 3). In this narrow temperature range we observe the phases

160   described in the Apollo "rusty rock", including troilite (FeS), lawrencite ($FeCl_2$) and wurtzite (ZnS).

161   Troilite (638-698 °C) forms platy crystals and occurs together with lawrencite (Fig. 3d). The troilite

162   plates have diameters of up to 200 μm. Lawrencite occurs over a wider temperature range of 538-

163   698 °C (Fig. 2). Where lawrencite coexists with troilite (Fig. 2d) the crystals are small, with prismatic

164   grains up to 10 μm in length. At slightly lower temperature (>638 °C) the lawrencite forms large platy

165   grains (Fig. 2e). Between 538 and 587 °C we observe a sharp boundary between a lawrencite and

166   wurtzite dominated section (Fig. 2f). In the wurtzite dominated section we observe occasional

167   triangular, platy $FeCl_2$ grains (Fig. 2g). The occurrence of wurtzite is limited to a narrow temperature

168   range of 538-587 °C (Fig. 3). The typical hexagonal shape of wurtzite is only occasionally observed,

169   but here we find that it forms dense aggregations of intergrown ZnS crystals (Fig. 2g). Below 538 °C

170   we only observe Zn-phases and no Cu- or Fe-bearing minerals. Below 498 °C the only phase

7

171　　observed is $ZnCl_2$ (Fig. 3). $ZnCl_2$ is highly deliquescent and rapidly absorbs enough water from the

172　　atmosphere to form an aqueous solution, once exposed to air. This process occurs within less than 5

173　　minutes in the relatively humid air of Münster in the summer, apparent in all samples where $ZnCl_2$ is

174　　present (Fig. 2i). Finally, in the transitional temperature range between 498 and 538 °C (Fig. 3) we

175　　observe an unidentified Zn-phase containing both S and Cl (Fig. 2h).

176　　　　**3.2 Metal reaction experiments**

177　　　　The Fe metal chips reacted with a C-O-S-Cl-Zn gas at 396, 496, 580, 708, 825 and 1005 °C,

178　　and the run products show that the reaction resulted in extensive reaction coatings with variable

179　　amounts of $FeCl_2$, (Zn,Fe)S and FeS. In Figures 4 and 5 we show backscattered electron images of the

180　　surface coatings on the metal chips and polished cross-sections of the coated Fe metal chips. With

181　　increasing temperature, the coatings become thicker and coarser grained (Fig. 5). This proved to be

182　　problematic during the sample polishing as the sulfide coatings partially decoupled from the

183　　underlying Fe metal chips.

184　　　　At 396 °C the coating almost exclusively contains $FeCl_2$ (lawrencite) which crystallized as

185　　prismatic crystals with lengths of up to 200 μm and thicknesses of up to 40 μm (Fig. 4a). On the

186　　surface coatings we did not observe any sulfide phase. In cross-section it's evident that the coatings

187　　are thin with thicknesses of up to 20 μm (Fig. 4b & a). In addition to lawrencite we also detected

188　　traces of (Zn,Fe)S. However, we could not observe individual grains, suggesting that they have

189　　diameters of less than 20 μm.

190　　　　At 496 °C lawrencite forms a dense and fine-grained coating on the reacted Fe metal (Fig.

191　　4d). Individual grains are small with diameters of less than 5 μm. In cross-section we observe that the

192　　coating is much thicker than at 396 °C, measuring up to 80 μm (Fig. 4e & f). We also observe reaction

193　　between the lawrencite and the epoxy resin in which the sample is embedded (Fig. 4f). This secondary

194　　alteration of the coating likely occurred during embedding in the liquid resin as it did not change once

195　　the resin hardened.

196   At 580 °C we observe $FeCl_2$ and $(Zn,Fe)S$ in the coating of the Fe metal chip (Fig. 4g). The

197   coating is fine-grained with individual $(Zn,Fe)S$ crystals with diameters of up to 8 μm. The coating

198   has partially engulfed silica glass fibers on which the Fe metal chip was placed (Fig. 4g). In cross-

199   section we observe that the coating with a thickness of up to 150 μm partially detached from the

200   metal, suggesting a poor cohesion (Fig. 4h & i). The coating appears to be layered, with the $FeCl_2$ on

201   the metal chip and the sulfide on the surface (Fig. 4i).

202   At 708 °C $(Zn,Fe)S$ dominates the coating and only traces of $FeCl_2$ are observed in cross-

203   section (Fig. 5 a-c). The sulfide grains have diameters of up to 40 μm (Fig. 5a), with a total coating

204   thickness of ~100 μm (Fig. 5b). Traces of $FeCl_2$ were detected in the coating by EDS, but individual

205   grains could not be identified unambiguously, suggesting grain sizes of less than 2 μm.

206   At 825 °C the coating only contains sulfides. It is the only sample where pure FeS could be

207   distinguished from $(Zn,Fe)S$. At the surface of the coating grains have diameters of up to 60 μm (Fig.

208   5d). The coating is dense and the individual sulfide crystals are euhedral. The coating is partially

209   detached from the underlying Fe metal chip (Fig. 5e), but in some sections the contact is observed.

210   The pure FeS is in direct contact with the metal chip and forms an undulatory interface (Fig. 5f). The

211    $(Zn,Fe)S$ occurs on the surface of the coating.

212   Finally, at 1005 °C the coating mainly consists of $(Fe,Zn)S$ (Fig. 5 g-i). The sulfide grains

213   have diameters of up to 50 μm. The coating thickness exceeds 200 μm and was mostly lost during

214   preparation of the cross-sections (Fig. 5h). The surface of the reacted Fe metal chip is highly

215   undulatory and porosity is observed to a depth of 200 μm (Fig. 5h & i). The pore space formed during

216   the reaction with the C-O-S-Cl-Zn gas and suggests a mobilization of Fe at 1005 °C. Indeed, apart

217   from $(Fe,Zn)S$ we also observe fayalite (Fe_2SiO_4) in the coating (Fig. 5g & i). The fayalite is primarily

218   located where the Fe metal chip was in contact with the silica glass wool or the wall of the silica glass

219   tube, facilitating the reaction.

220   In summary, 580 °C is the only temperature at which both $FeCl_2$ and $(Zn,Fe)S$ could be

221   observed abundantly in the coatings. At lower temperatures only traces of sulfide could be detected in

222   the coatings, whereas at 708 °C only traces of $FeCl_2$ were detected. At even higher temperatures (825,

223   1005 °C) chlorides are absent from the coatings.

4. Discussion

225   Both the "gas deposition experiments" and the "metal reaction experiments" result in the

226   formation of mineral assemblages containing sulfides and chlorides, and both experimental

227   approaches reproduce the fumarolic alteration observed in the lunar Apollo 16 "rusty rock" 66095. In

228   the gas deposition experiments FeS, $FeCl_2$ and ZnS occur over the temperature range of 538-638 °C.

229   In the metal reaction experiment the most extensive reaction and formation of both (Zn,Fe)S and

230      $FeCl_2$ occurred at 580 °C, which is an almost identical temperature range as the gas deposition

231   experiment. The two experiments suggest that 580 ± 50 °C is the temperature condition under which

232   fumarolic alteration occurred on the Moon, as recorded in the "rusty rock" samples.

233   In our high temperature experiments we did not observe any oxyhydroxides and oxides that

234   have been reported in the Apollo "rusty rock" samples, such as akaganéite (β-FeO(OH,Cl)), goethite

235   (α-FeO(OH)) or hematite (α-Fe_2O_3) (Shearer et al., 2014). We conducted our experiments with water

236   free, dried reagents, because a reliable control of fH_2 in the evacuated silica glass tubes was not

237   possible. However, our experiments have consistently reproduced the dry alteration phases observed

238   in the "rusty rock". This suggests, that the oxyhydroxides are a secondary alteration product of the

239   primary $FeCl_2$ formed at high temperature. The textural evidence from the Apollo 16 sample suggests

240   that oxyhydration did not form upon exposure to a terrestrial atmosphere, but that akaganéite did

241   replace lawrencite, based on the Cl-isotopes (Shearer et al., 2014). This suggests that the initial

242   fumarolic alteration phase at 580 ± 50 °C was followed by a secondary alteration phase at lower

243   temperatures and with a gas at higher fH_2 and fH_2O.

244   We performed our experiments in sealed and evacuated silica tubes with a 900 °C

245   temperature range. In such an experimental setup the direct control of gas fugacities (e.g. fO_2 and fS_2)

246   is not possible in the same way as in a conventional gas mixing furnace. Furthermore, the gas

247   fugacities may vary along the temperature gradient, as well as over time as phases are deposited from

248   the gas phase or gas species are bound to solids via chemisorption (King et al., 2018; Nekvasil et al.,

249   2019). In addition, gas-solid reaction experiments may be kinetically limited (Renggli and King,

250   2018). However, some first order estimates are made based on the phases observed in the experiments

251   and in the lunar "rusty rock".

252   **4.1 Constraints on the gas phase composition**

253   The starting material used in our experiments contained graphite powder (Table 1) and were

254   placed in graphite crucibles. Graphite acts as a strong reducing agent and buffers the fO_2 at the source

255   at 1250 °C at the C-CO buffer ($\log fO_2$ = -16.84). This is in analogy to the formation of CO-rich lunar

256   volcanic gas that forms by the oxidation of graphite (Fogel and Rutherford, 1995; Nicholis and

257   Rutherford, 2009). The CO gas further forms gaseous Zn and oxygen due to the decomposition of

258   ZnO. A second decomposition reaction may follow the equation $ZnO + MgCl_2 = ZnCl_{2(g)} + MgO$,

259   but this does not directly impinge on the oxygen fugacity.

260   At lower temperatures gas compositions, or gas fugacities, are assessed based on the phase

261   assemblages observed in the experiments and the lunar "rusty rock". First, we discuss the "gas

262   deposition experiments". All chalcocite crystals deposited between 880-1140 °C show the growth of

263   Cu metal whiskers on the surface (Fig. 2a &b). Metal whiskers on sulfides are an indication of a

264   decrease in fS_2 after the formation of the sulfides in a low pressure environment (Wagner, 1952;

265   Nicolle and Rist, 1979). For example, iron whiskers were observed on sulfide grains in samples from

266   asteroid 25143 Itokawa, sampled by Hayabusa (Matsumoto et al., 2020). The observation of Cu metal

267   whiskers on the Cu_2S grains illustrates that the gas fugacities in our runs are not constant over time.

268   Initially, the Zn-Cu-Fe-C-O-S-Cl compounds in the source volatilize rapidly which results in

269   increasing gas pressure in the silica glass tube. As sulfides and chlorides deposit from the gas phase

270   along the temperature gradient the gas pressure decreases again. The sole species remaining

271   abundantly in the gas phase is CO, buffered by the excess graphite in the source at 1250 °C. We

272   therefore assume that $\log fO_2$ remains constant with time, but $\log fS_2$ decreases as the sulfides are

273   deposited. The formation of the Cu metal whiskers suggests that $\log fS_2$ drops to the phase boundary of

274   Cu_2S and Cu in the $\log fS_2$-$\log fO_2$ space, as indicated by the arrow in Figure 6a.

275   The occurrence of FeS and $FeCl_2$ together in both experimental approaches in the temperature

276   range 580 ± 50 °C, which we identified as the temperature condition forming the "rusty rock"

277   alteration on the Moon, allows further constraints of $\log fS_2$ and $\log fCl_2$ in the experiment and for the

278   lunar "rusty rock". The presence of both FeS and $FeCl_2$ (Fig. 2d for the gas deposition experiment and

279   Fig. 4i for the metal reaction experiment) constrains the two variables to the univariate line indicated

280   in Figure 6b. At 600 °C $\log fS_2$ is in the range of -13.2 to -10.5 and $\log fCl_2$ is in the range of -13.9

281   to -12.5 (Fig. 6b).

282   Finally, in the Fe "metal reaction experiments" the oxygen fugacity is further buffered by Fe

283   metal at every temperature. As we did not observe any wüstite (FeO) in the experiments, we conclude

284   that the $\log fO_2$ remained below the iron-wüstite (IW) buffer at all temperatures and for the entire

285   duration of the experiment, which is in good agreement with the estimates for the redox conditions on

286   the Moon between IW and IW-2.5 (Fogel and Rutherford, 1995; Nicholis and Rutherford, 2009).

287   Recent calculations of a lunar volcanic gas phase revealed that main gas species are S_2, CO

288   and H_2 at 1200 °C, 10^{-6} bar and reducing conditions of IW-2 (Renggli et al., 2017). This model was

289   based on measurements of the volatiles H, S, Cl, F and C in partially degassed lunar pyroclastic glass

290   beads (Saal et al., 2008; Wetzel et al., 2015). In such a volcanic gas composition the metals primarily

291   deposit as sulfides with only minor abundances of elemental metal. Zink, Fe, Ni and Cu were

292   observed as sulfides in coatings on the pyroclastic glass beads and the only chloride that was observed

293   was NaCl (Butler and Meyer, 1976; Wasson et al., 1976; Clanton et al., 1978; Cirlin and Housley,

294   1979). Iron and Zn-chlorides, as observed in the Apollo 16 "rusty rock", and in our experiments, are

295   not predicted as deposited solids in the thermodynamic model and were not observed in pyroclastic

296   glass bead coatings (Renggli et al., 2017). As a consequence, we suggest that the gas composition

297   forming the "rusty rock" alteration had a different composition. Specifically, the $\log fCl_2$ must have

298   been orders of magnitude higher compared to the pyroclastic gas, allowing the deposition of metal

299   chlorides from the gas phase and the reaction of Fe metal in the host rock to chloride. Commonly used

300   50% condensation temperatures (Lodders, 2003) suggest deposition of Fe above 1300 °C (Day et al.,

301   2019). However, our experimental results showed that $FeCl_2$ are deposited from a gas phase at

302   temperatures as low as 540 °C. This underlines the importance of experimental exploration of a

303   broader range of gas compositions from which metals deposit and condensate in planetary

304   environments.

305   Note that the sulfide mineralization was not just observed in the Apollo 16 "rusty rock" but

306   sulfides have been observed in other Apollo 16 samples, including 67016 (Norman, 1981; Norman et

307   al., 1995; Shearer et al., 2012), as well as Apollo 11, 14 and 17 rocks (McKay et al., 1972; Ramdohr,

308   1972; Elardo et al., 2012). However, these rocks do not show chloride alteration and the predominant

309   sulfide phase is troilite (Shearer et al., 2012). In our experiment troilite was deposited from the gas

310   phase at 638-698 °C (Fig. 3). In addition to sulfide veins, likely deposited from a reducing S-rich gas,

311   troilite also occurs in metasomatic replacement textures of olivine to troilite and low-Ca pyroxene

312   (Colson, 1992; Norman et al., 1995; Shearer et al., 2012). In an ongoing study we will further

313   investigate the conditions under which these metasomatic replacement reactions occurred. At more

314   oxidizing conditions sulfates rapidly form when SO_2 reacts with basaltic glasses and minerals (King et

315   al., 2018; Renggli et al., 2019a). At reducing conditions relevant to the Moon and Mercury (Blewett et

316   al., 2013; Nittler et al., 2014) sulfides are predicted to form in a S-rich environment. At 700 °C and an

317   oxygen fugacity <IW additional sulfides may form including Na-, Ca- and Mg-sulfides (Renggli et al.,

318   2019b).

5. Conclusions

320   We conducted gas deposition and metal reaction experiments to simulate fumarolic alteration

321   in the Apollo 16 "rusty rock" 66095. The silica glass tube experiments are a useful tool to explore

322   metal transport processes and gas-solid reactions, such as sulfidation processes.

323   Our experiments indicate that the observed mineral assemblage of the rusty rock was formed

324   at 580 ± 50 °C.

325   In this temperature range we observed the deposition of $FeCl_2$, ZnS and FeS in the gas

326   deposition experiment, and the formation of $FeCl_2$ and (Zn,Fe)S coatings on Fe metal grains reacted

327   with a Zn-C-O-S-Cl gas.

328   The gas deposition experiments also showed that Cu_2S was deposited at higher temperatures

329   above 880 °C. If Cu was carried in the lunar fumarolic gas, it must have been deposited at higher

330   temperatures and therefore likely at greater depths in the lunar crust.

331   The observed assemblage of $FeCl_2$ and FeS allowed us to constrain sulfur and chlorine

332   fugacities in the gas phase at reducing conditions below the IW buffer.

Acknowledgments

References

340   Blewett D. T., Vaughan W. M., Xiao Z., Chabot N. L., Denevi B. W., Ernst C. M., Helbert J.,
341   D'Amore M., Maturilli A., Head J. W. and Solomon S. C. (2013) Mercury's hollows:
342   Constraints on formation and composition from analysis of geological setting and spectral
343   reflectance. *J. Geophys. Res. Planets* **118**, 1013–1032.

344   Butler P. and Meyer C. (1976) Sulfur prevails in coatings on glass droplets - Apollo 15 green and
345   brown glasses and Apollo 17 orange and black (devitrified) glasses. *Proc. Lunar Sci. Conf.* **7**,
346   1561–1581.

347   Chase M. W. (1998) *NIST-JANAF Thermochemical Tables*. 4th ed., Physical and Chemical Reference
348   Data.

349   Cirlin E. H. and Housley R. M. (1979) Scanning Auger Microprobe and atomic absorption studies of
350   lunar volcanic volatiles. In Planetary Science Conference Proceedings. pp. 341–354.

351   Clanton U. S., McKay D. S., Waits G. and Fuhrman R. (1978) Sublimate morphology on 74001 and
352   74002 orange and black glassy droplets. *Lunar Planet. Sci. Conf.* **9**, 1945–1957.

353   Colson R. O. (1992) Mineralization on the Moon?: Theoretical Considerations of Apollo 16 "Rusty
354   Rocks," Sulfide Replacement in 67016, and Surface-Correlated Volatiles on Lunar Volcanic
355   Glass. *Proc. Lunar Planet. Sci.* **22**, 427–436.

356   Dalby K. N., Berger J. A., Brand H. E. A., Cairney J. M., Eder K., Eggins S. M., Herring A., Hervig
357   R. L., Krieder P. B., Mernagh T. P., Palm A. B., Renggli C. J., Troitzsch U., Yue L. and King
358   P. L. (2018) Analytical Techniques for Probing Small-Scale Layers that Preserve Information
359   on Gas–Solid Interactions. *Rev. Mineral. Geochem.* **84**, 103–175.

Day J. M. D., Moynier F. and Shearer C. K. (2017) Late-stage magmatic outgassing from a volatile-depleted Moon. *Proc. Natl. Acad. Sci.*, 201708236.

Day J. M. D., Sossi P. A., Shearer C. K. and Moynier F. (2019) Volatile distributions in and on the Moon revealed by Cu and Fe isotopes in the 'Rusty Rock' 66095. *Geochim. Cosmochim. Acta*, S0016703719301218.

El Goresy A., Ramdohr P., Pavićević M., Medenbach O., Müller O. and Gentner W. (1973) Zinc, lead, chlorine and FeOOH-bearing assemblages in the Apollo 16 sample 66095: Origin by impact of a comet or a carbonaceous chondrite? *Earth Planet. Sci. Lett.* **18**, 411–419.

Elardo S. M., McCubbin F. M. and Shearer C. K. (2012) Chromite symplectites in Mg-suite troctolite 76535 as evidence for infiltration metasomatism of a lunar layered intrusion. *Geochim. Cosmochim. Acta* **87**, 154–177.

Fogel R. A. and Rutherford M. J. (1995) Magmatic volatiles in primitive lunar glasses: I. FTIR and EPMA analyses of Apollo 15 green and yellow glasses and revision of the volatile-assisted fire-fountain theory. *Geochim. Cosmochim. Acta* **59**, 201–215.

Hunter R. H. and Taylor L. A. (1981a) Rust and schreibersite in Apollo 16 highland rocks: Manifestations of volatile-element mobility. In *Lunar and Planetary Science Conference Proceedings* 253-259.

Hunter R. H. and Taylor L. A. (1981b) Rusty Rock 66095: A paradigm for volatile-element mobility in highland rocks. In *Lunar and Planetary Science Conference Proceedings*

Jean M. M., Bonder B., Farley C. and Taylor L. A. (2016) "Rusty Rocks" from the Moon: Volatile-Element Contributions from Meteorites. In Lunar and Planetary Science Conference. p. 2498. Available at: http://adsabs.harvard.edu/abs/2016LPI....47.2498J [Accessed August 7, 2019].

Kerridge J. F., Kaplan I. R., Petrowski C. and Chang S. (1975) Light element geochemistry of the Apollo 16 site. *Geochim. Cosmochim. Acta* **39**, 137–162.

King P. L., Wheeler V. M., Renggli C. J., Palm A. B., Wilson S. A., Harrison A. L., Morgan B., Nekvasil H., Troitzsch U., Mernagh T., Yue L., Bayon A., DiFrancesco N. J., Baile R., Kreider P. and Lipi W. (2018) Gas–Solid Reactions: Theory, Experiments and Case Studies Relevant to Earth and Planetary Processes. *Rev. Mineral. Geochem.* **84**, 1–56.

Krähenbühl U., Ganapathy R., Morgan J. A. and Anders E. (1973) Volatile elements in Apollo 16 samples: implications for highland volcanism and accretion history of the moon. In *Proceedings of the 4th Lunar Science Conference.* Pergamon Press, New York. pp. 1325–1348.

Lodders K. (2003) Solar System Abundances and Condensation Temperatures of the Elements. *Astrophys. J.* **591**, 1220.

Matsumoto T., Harries D., Langenhorst F., Miyake A. and Noguchi T. (2020) Iron whiskers on asteroid Itokawa indicate sulfide destruction by space weathering. *Nat. Commun.* **11**, 1–8.

McCubbin F. M., Kaaden K. E. V., Tartèse R., Klima R. L., Liu Y., Mortimer J., Barnes J. J., Shearer C. K., Treiman A. H., Lawrence D. J., Elardo S. M., Hurley D. M., Boyce J. W. and Anand M. (2015) Magmatic volatiles (H, C, N, F, S, Cl) in the lunar mantle, crust, and regolith: Abundances, distributions, processes, and reservoirs. *Am. Mineral.* **100**, 1668–1707.

McKay D. S., Clanton U. S., Morrison D. A. and Ladle, G.H. (1972) Vapor phase crystallization in Apollo 14 breccia. In *Proceedings of the Third Lunar Science Conference* pp. 739–752.

Meyer C. (2009) 66095 "Rusty Rock." *Lunar Sample Compend.*, 22.

Nekvasil H., DiFrancesco N. J., Rogers A. D., Coraor A. E. and King P. L. (2019) Vapor-Deposited Minerals Contributed to the Martian Surface During Magmatic Degassing. *J. Geophys. Res. Planets* **124**, 1592–1617.

Nicholis M. G. and Rutherford M. J. (2009) Graphite oxidation in the Apollo 17 orange glass magma: Implications for the generation of a lunar volcanic gas phase. *Geochim. Cosmochim. Acta* **73**, 5905–5917.

Nicolle R. and Rist A. (1979) The mechanism of whisker growth in the reduction of wüstite. *Metall. Trans. B* **10**, 429–438.

Nittler L. R., Weider S. Z., Starr R. D., Chabot N., Denevi B. W., Ernst C. M., Goudge T. A., Head J. W., Helbert J., Klima R. L., McCoy T. J. and Solomon S. C. (2014) Sulfur-Depleted Composition of Mercury's Largest Pyroclastic Deposit: Implications for Explosive Volcanism and Surface Reflectance on the Innermost Planet. *Lunar Planet. Sci. Conf.* **45**, 1391.

Norman M. D. (1981) Petrology of suevitic lunar breccia 67016. In *Proc. Lunar Plaent. Sci.* pp. 235–252.

Norman M. D., Keil K., Griffin W. L. and Ryan C. G. (1995) Fragments of ancient lunar crust: Petrology and geochemistry of ferroan noritic anorthosites from the Descartes region of the Moon. *Geochim. Cosmochim. Acta* **59**, 831–847.

Norris C. A. and Wood B. J. (2017) Earth's volatile contents established by melting and vaporization. *Nature* **549**, 507–510.

Ramdohr P. (1972) Lunar pentlandite and sulfidization reactions in microbreccia 14315, 9. *Earth Planet. Sci. Lett.* **15**, 113–115.

Renggli C. J. and King P. L. (2018) SO2 Gas Reactions with Silicate Glasses. *Rev. Mineral. Geochem.* **84**, 229–255.

Renggli C. J., King P. L., Henley R. W. and Norman M. D. (2017) Volcanic gas composition, metal dispersion and deposition during explosive volcanic eruptions on the Moon. *Geochim. Cosmochim. Acta* **206**, 296–311.

Renggli, King P. L., Henley R. W., Guagliardo P., McMorrow L., Middleton J. P. and Turner M. (2019a) An experimental study of SO2 reactions with silicate glasses and supercooled melts in the system anorthite–diopside–albite at high temperature. *Contrib. Mineral. Petrol.* **174**, 3.

Renggli, Palm A. B., King P. L. and Guagliardo P. (2019b) Implications of Reactions Between SO2 and Basaltic Glasses for the Mineralogy of Planetary Crusts. *J. Geophys. Res. Planets* **124**, 2563–2582.

Roine A. (2015) *Outotec HSC Chemistry 8.1.*, Outotec Research Center, Finland.

Saal A. E., Hauri E. H., Cascio M. L., Van Orman J. A., Rutherford M. C. and Cooper R. F. (2008) Volatile content of lunar volcanic glasses and the presence of water in the Moon's interior. *Nature* **454**, 192–195.

439   Sharp Z. D., Shearer C. K., McKeegan K. D., Barnes J. D. and Wang Y. Q. (2010) The Chlorine
440   Isotope Composition of the Moon and Implications for an Anhydrous Mantle. *Science* **329**,
441   1050–1053.

442   Shearer C. K., Burger P. V., Guan Y., Papike J. J., Sutton S. R. and Atudorei N.-V. (2012) Origin of
443   sulfide replacement textures in lunar breccias. Implications for vapor element transport in the
444   lunar crust. *Geochim. Cosmochim. Acta* **83**, 138–158.

445   Shearer C. K., Sharp Z. D., Burger P. V., McCubbin F. M., Provencio P. P., Brearley A. J. and Steele
446   A. (2014) Chlorine distribution and its isotopic composition in "rusty rock" 66095.
447   Implications for volatile element enrichments of "rusty rock" and lunar soils, origin of "rusty"
448   alteration, and volatile element behavior on the Moon. *Geochim. Cosmochim. Acta* **139**, 411–
449   433.

450   Sossi P. A. and Fegley B. (2018) Thermodynamics of Element Volatility and its Application to
451   Planetary Processes. *Rev. Mineral. Geochem.* **84**, 393–459.

452   Sossi P. A., Klemme S., O'Neill H. St. C., Berndt J. and Moynier F. (2019) Evaporation of
453   moderately volatile elements from silicate melts: experiments and theory. *Geochim.*
454   *Cosmochim. Acta* **260**, 204–231.

455   Taylor L. A., Mao H. K. and Bell P. M. (1974) Identification of the Hydrated Iron Oxide Mineral
456   Akaganéite in Apollo 16 Lunar Rocks. *Geology* **2**, 429–432.

457   Taylor L. A., Mao H. K. and Bell P. M. (1973) "Rust" in the Apollo 16 rocks. In *Proc. 4th Lunar Sci.*
458   *Conf.* pp. 829–839.

459   Wagner C. (1952) Mechanism of the Reduction of Oxides and Sulphides to Metals. *JOM* **4**, 214–216.

460   Wang Y., Guan Y., Hsu W. and Eiler J. M. (2012) Water Content, Chlorine and Hydrogen Isotope
461   Compositions of Lunar Apatite. *Meteorit. Planet. Sci. Suppl.* **75**, 5170.

462   Wasson J. T., Boynton W. V., Kallemeyn G. W., Sundberg L. L. and Wai C. M. (1976) Volatile
463   compounds released during lunar lava fountaining. *Proc. Lunar Sci. Conf.* **7**, 1583–1595.

464   Wetzel D. T., Hauri E. H., Saal A. E. and Rutherford M. J. (2015) Carbon content and degassing
465   history of the lunar volcanic glasses. *Nat. Geosci.* **8**, 755–758.

466

467

468 **Tables**

469   *Table 1: Composition of the experimental charges of the gas deposition and metal reaction*
470 *experiments. The table shows nominal molar concentrations of the reagent mixtures and weighed-in*
471 *values.*

	Gas deposition experiment		Metal reaction experiment	
	Molar abundances	Weight g	Molar abundances	Weight g
ZnO	1	0.0068	1	0.0158
FeS	1	0.0073	-	-
CuS	1	0.0080	-	-
MgCl$_2$	3	0.0239	1	0.0185
S	-	-	1	0.0062
C	4	0.0040	4	0.0094
Total		0.05		0.05

472

473   *Table 2: Experimental conditions and positions of Fe metal chips along the silica tube in the*
474 *metal reaction experiment. Temperatures were measured with a type B thermocouple in the vertical*
475 *tube furnace in 1 cm steps prior to the experiments.*

	Distance from top of tube	Temperature
	cm	°C
a	7	396
b	11	496
c	13	580
d	15	708
e	17	825
f	21	1005
Volatile source	31	1250
Tube length		28 cm
Duration		24h

476
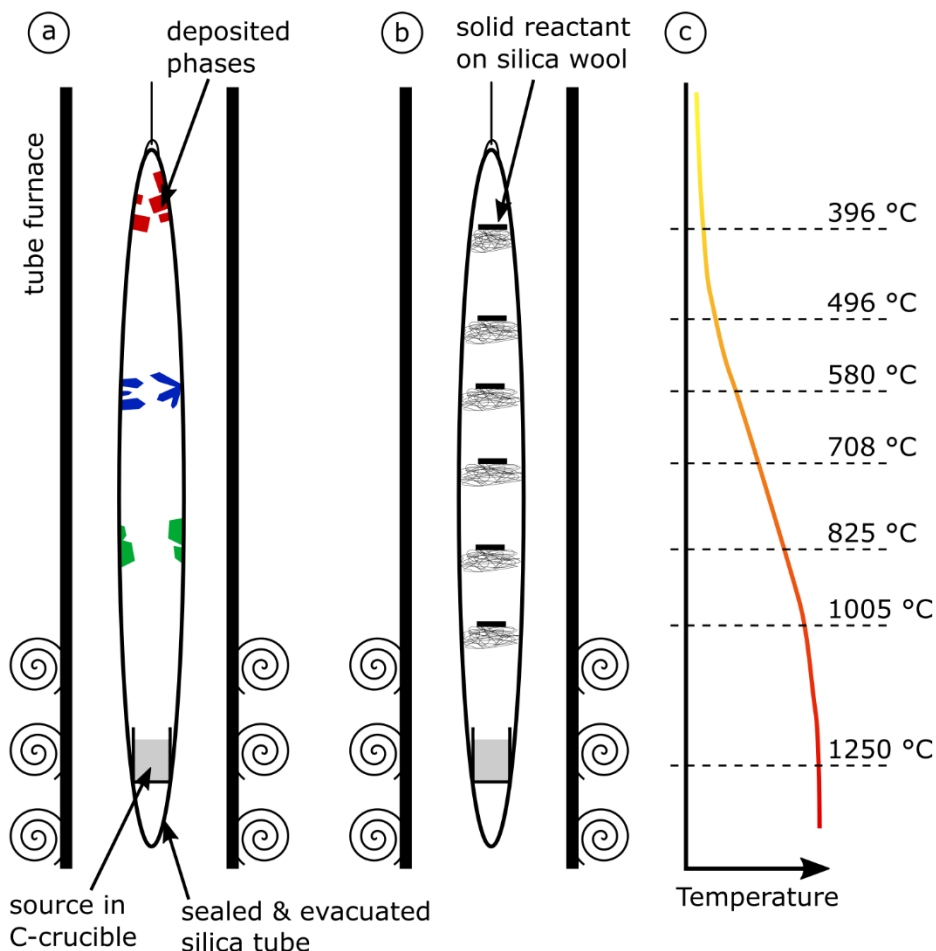
Figures

Figure 1: Illustration of the experimental setup in a vertical tube furnace. a) Gas deposition experiment. The source in the hot zone of the furnace volatilizes and different phases are deposited along the temperature gradient within the silica glass tube.; b) Metal reaction experiment. The Fe metal chips were placed on SiO_2 glass wool spacers at 396, 496, 580, 708, 825 and 1005 °C; c) schematic of the furnace temperature gradient with temperatures at which the Fe metal chips were placed within the tube.
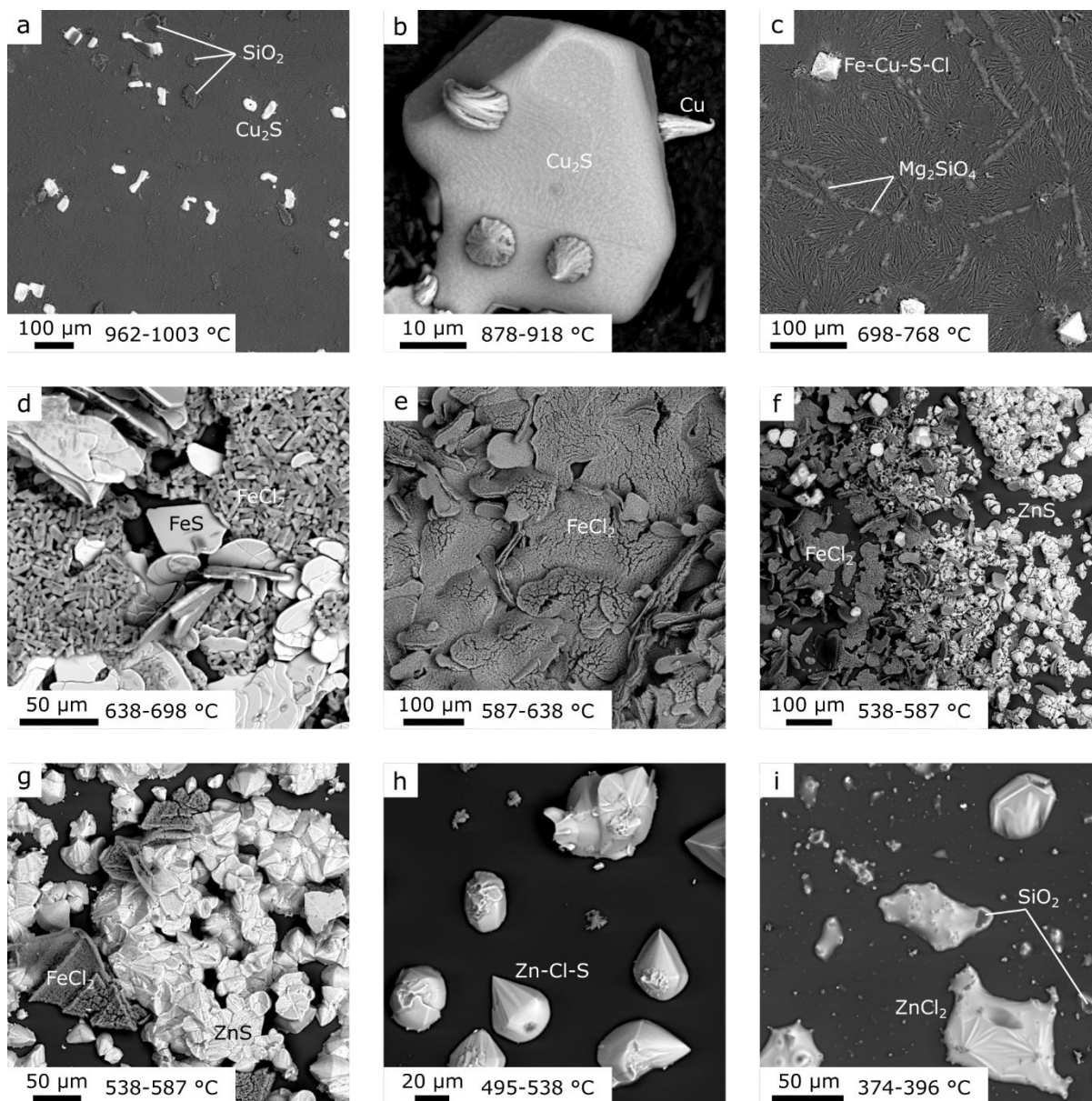
Figure 2: Backscattered electron images of phases deposited on the inner silica tube wall ("gas deposition experiment"). a) Cu_2S grains and SiO_2 glass dust which was formed during opening of the tube, 962-1003 °C; b) Cu_2S grain with Cu metal whiskers, 878-918 °C; c) Unidentified Fe-Cu-S-Cl phase and Mg_2SiO_4, the reaction product of MgO with the silica glass tube wall, 698-768 °C; d) FeS and $FeCl_2$, 638-698 °C; e) $FeCl_2$, 587-638 °C; f) $FeCl_2$ and ZnS, 538-587 °C; g) $FeCl_2$ and ZnS, 538-587 °C; h) Unidentified Zn-Cl-S phase, 495-538 °C; i) Liquidized and hydrated $ZnCl_2$ due to its deliquescence, SiO_2 glass shards, 374-396 °C.

493
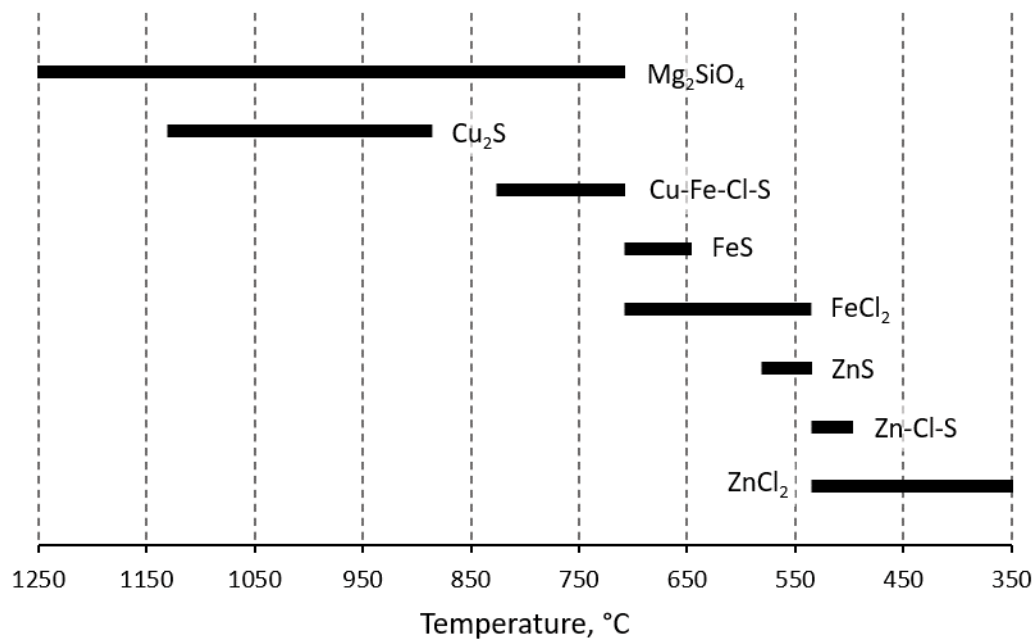
Figure 3: Distribution of phases deposited along the temperature gradient in the silica tube summarizing the observations shown in Fig. 2 from the gas deposition experiment. The solid bars show the temperature ranges over which the respective phases were observed in the silica glass tube. "Rusty rock" phases are observed over the temperature range 538-638 °C.

Surface Cross-section Cross-section

396 °C

496 °C

580 °C

499
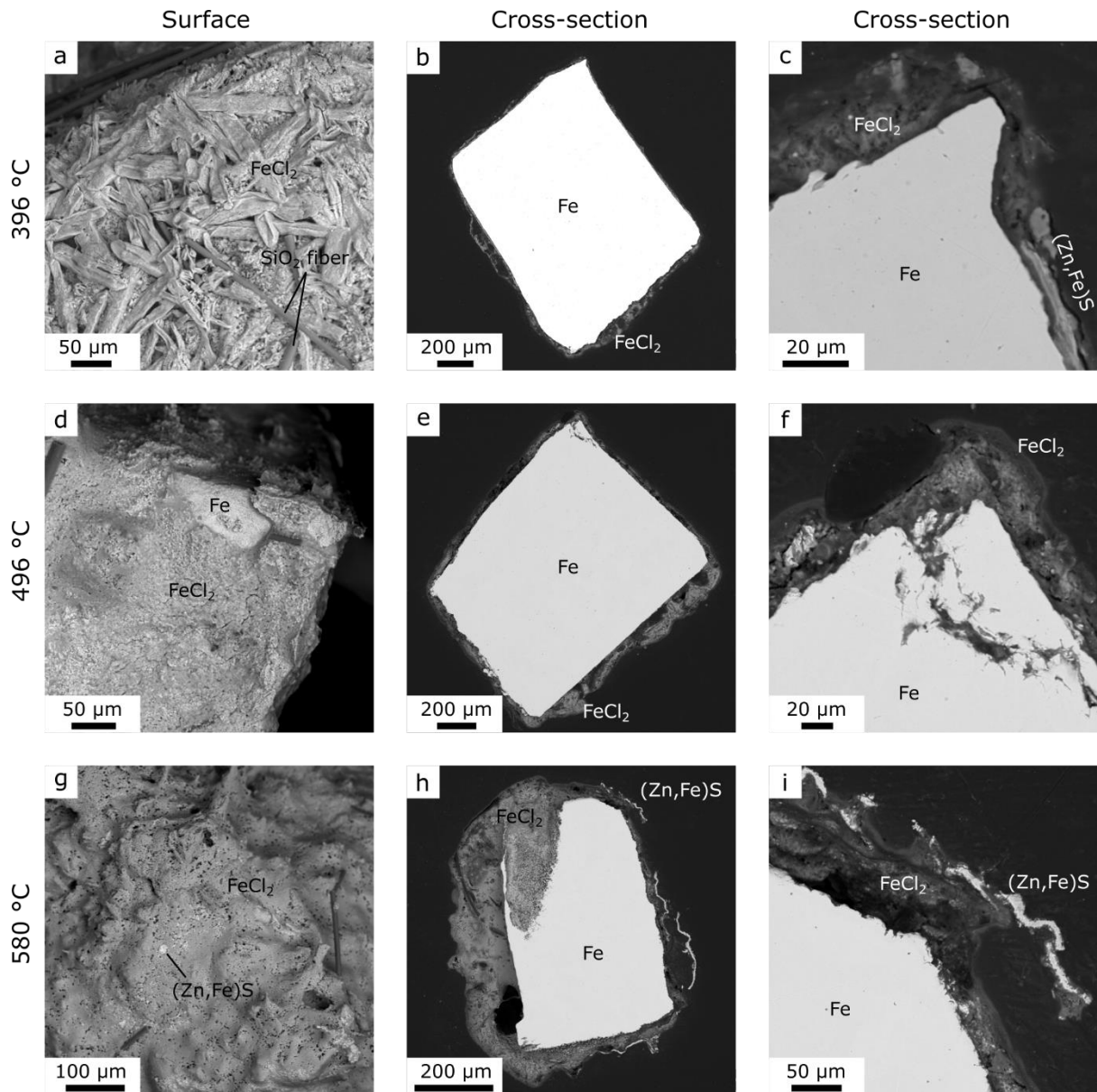
Figure 4: Backscattered electron images of the Fe metal reaction experiment. Images a, d and c show the surfaces of the coatings and images b, c, e, f, h and I show cross-sections of the samples. The rows indicate the temperatures, 396 °C (a-c), 496 °C (d-f) and 580 °C (g-h).

503
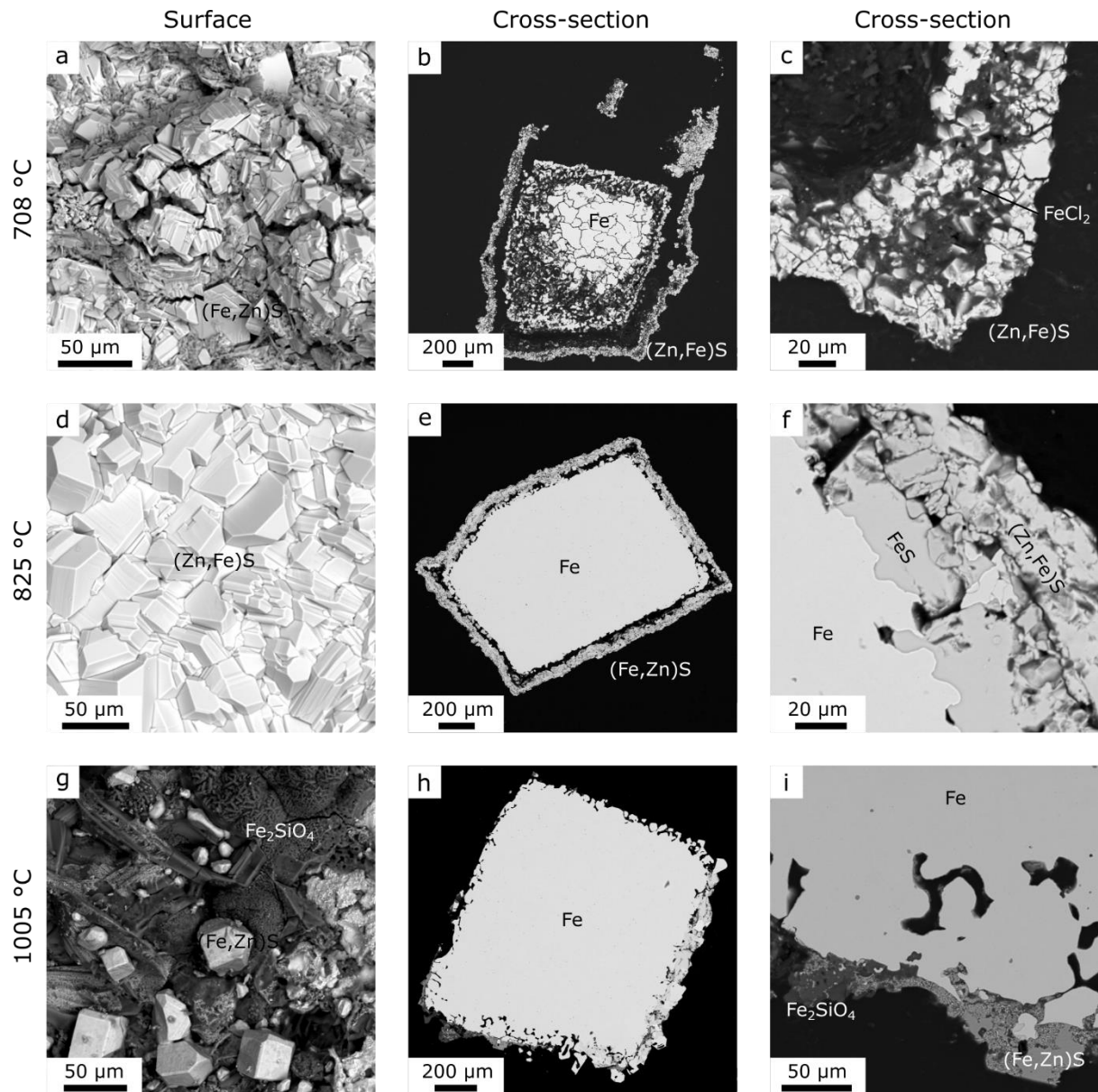
Figure 5: Backscattered electron images of the Fe metal reaction experiment. Images a, d and c show the surfaces of the coatings and images b, c, e, f, h and I show cross-sections of the samples. The rows indicate the temperatures, 708 °C (a-c), 825 °C (d-f) and 1005 °C (g-h).

510
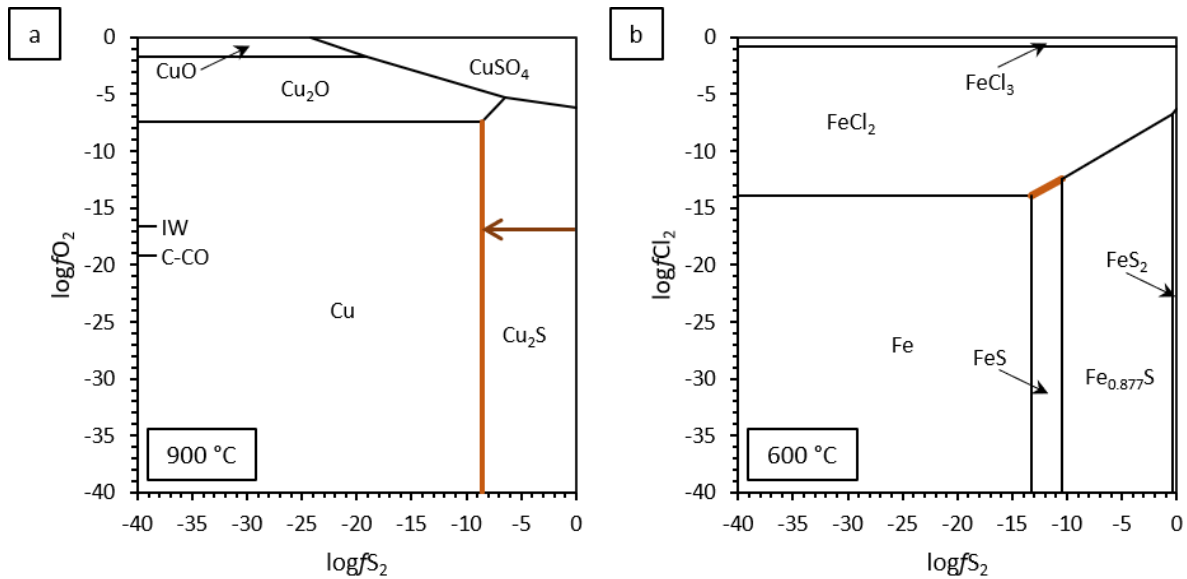
Figure 6: a) Phase stability diagram of the system Cu-S-O as a function of logfS$_2$ and logfO$_2$ at 900 °C, 1 bar. The univariate line in brown shows the condition for coexistence of Cu and Cu$_2$S as observed in the metal transport experiment and the formation of Cu whiskers on the Cu$_2$S crystal. The brown arrow indicates a decrease in logfS$_2$ with experimental duration resulting in the growth of Cu whiskers. b) Phase stability diagram of the system Fe-S-Cl as a function of log fS$_2$ and logfCl$_2$ at 600 °C, 1 bar. The univariate line shows the co-stability of FeCl$_2$ and FeS as observed in the metal transport experiment at 638-698 °C (Fig. 2d) and the Fe metal-gas reaction experiment at 580 °C (Fig. 4g-i). Calculations were made with the program HSC9 by Outotec, largely based on data from the NIST-JANAF thermochemical data base (Chase, 1998; Roine, 2015).